SCIENTIFIC REPORTS

OPEN

SUBJECT AREAS:
ELECTROCATALYSIS
FUEL CELLS
NANOPARTICLES
GRAPHENE

Received
31 January 2013

Accepted
15 April 2013

Published
3 May 2013

Correspondence and requests for materials should be addressed to G.A.B. (gbotton@mcmaster.ca); T.-K.S. (tsham@uwo.ca) or X.L.S. (xsun@eng.uwo.ca)

Single-atom Catalysis Using Pt/Graphene Achieved through Atomic Layer Deposition

Shuhui Sun[1,2], Gaixia Zhang[1,2], Nicolas Gauquelin[3,4], Ning Chen[5], Jigang Zhou[5], Songlan Yang[5], Weifeng Chen[5], Xiangbo Meng[1], Dongsheng Geng[1], Mohammad N. Banis[1], Ruying Li[1], Siyu Ye[6], Shanna Knights[6], Gianluigi A. Botton[3,4,7], Tsun-Kong Sham[8] & Xueliang Sun[1]

[1]Department of Mechanical and Materials Engineering, the University of Western Ontario, London, Ontario, N6A 5B9, Canada, [2]Institut National de la Recherche Scientifique-Énergie, Matériaux et Télécommunications, Varennes, QC J3X 1S2, Canada, [3]Canadian Centre for Electron Microscopy, McMaster University, Hamilton L8S 4M1, Canada, [4]Brockhouse Institute for Materials Research, McMaster University, Hamilton L9S 4M1, Canada, [5]Canadian Light Source, Saskatoon S7N 0X4, Canada, [6]Ballard Power Systems Inc., Burnaby, V5J 5J8, Canada, [7]Department of Materials Science and Engineering, McMaster University, Hamilton L8S 4L7, Canada, [8]Department of Chemistry, University of Western Ontario, London N6A 5B7, Canada.

Platinum-nanoparticle-based catalysts are widely used in many important chemical processes and automobile industries. Downsizing catalyst nanoparticles to single atoms is highly desirable to maximize their use efficiency, however, very challenging. Here we report a practical synthesis for isolated single Pt atoms anchored to graphene nanosheet using the atomic layer deposition (ALD) technique. ALD offers the capability of precise control of catalyst size span from single atom, subnanometer cluster to nanoparticle. The single-atom catalysts exhibit significantly improved catalytic activity (up to 10 times) over that of the state-of-the-art commercial Pt/C catalyst. X-ray absorption fine structure (XAFS) analyses reveal that the low-coordination and partially unoccupied densities of states of 5d orbital of Pt atoms are responsible for the excellent performance. This work is anticipated to form the basis for the exploration of a next generation of highly efficient single-atom catalysts for various applications.

Due to rising global energy demands, depletion of fossil fuel reserves, and environmental pollution problems, there is great interest in developing different kinds of high-efficient and low-cost renewable energy technologies, such as fuel cells, as a replacement for combustion-based energy sources[1]. Among the multitude of fuel cell technologies available, the direct methanol fuel cell (DMFC) has drawn much attention because of its eco-friendly system, high efficiency, high power density and short start-up transient-response time[2]. DMFC has thus been identified as a promising candidate to compete with the conventional batteries for powering portable electronic devices[3]. Methanol, a liquid at room temperature, makes storage and transport much easier. The theoretical potential for the standard methanol fuel cell is 1.25 V, which is close to that for hydrogen fuel cell. Furthermore the theoretical energy density of methanol fuel cell is 6.1 kWh/kg[4], 10 times higher than that of lithium-ion battery[5], which is a critical factor in the transportation sector.

Despite considerable advances in recent years, the widespread application of DMFC is hindered by several technical and economical barriers. Poor electrocatalytic activity toward methanol oxidation reaction (MOR) and serious CO poising of Pt catalyst at the anode[6] are the most severe challenges. For standard DMFC, Pt-based nanoparticles (2–5 nm) supported on carbon black are most commonly employed as the anode catalyst because of their excellent performance in MOR. Although Pt is efficient, it can be the most expensive component. Thus researchers have been trying to reduce the diameters of Pt nanoparticles to as small as 1 nm in order to increase the active surface area of the catalyst, and therefore to increase the catalytic activity of Pt in fuel cells. Downsizing Pt nanoparticles to clusters or even single atoms could significantly increase their catalytic activity and is therefore highly desirable to maximize the efficiency[7]. Since the first practical single-atom catalyst, which consists of only isolated single Pt atoms on FeO_x, was reported by Zhang and his collaborators[7], "single-atom catalysis" has attracted much more attention. However, the large-scale synthesis of practical and stable clusters and single atoms of catalysts remains a significant challenge because clusters and single atoms are too mobile and easy to sinter under realistic reaction conditions[8]. To this end, atomic layer deposition (ALD), a promising technique for small-size catalyst fabrication[9], provides the solution. In the ALD process, a substrate is alternately exposed to different

reactive precursor vapours, which react in a self-limiting manner to deposit materials in an atomic layer-by-layer fashion. Previous studies have revealed that ALD allows one to control the morphology of the deposited metal, from discrete tiny nanoparticles to a continuous thin film, through the surface chemistry[10,11].

In a conventional system, carbon black is commonly used as the support for Pt nanoparticle catalyst[12]. This system is intrinsically limited in terms of life span, and the catalytic surface area of the electrode tends to decrease with time due to the corrosion of the carbon black support. Recently, due to their unique electric and micro-structural characteristics, nanostructured carbon materials with graphene structures such as carbon nanotubes (CNTs) and carbon nanofibers (CNFs) have been studied extensively as alternative supports for electrocatalysts, showing much enhanced fuel cell performance[13]. Graphene, a unique structure of a two-dimensional (2D) sheet composed of sp^2-bonded carbon atoms with one-atomic layer thick, has inspired a flurry of interests for both fundamental science and applied research due to its extraordinary properties[14]. One hopes to employ such 2-D sheets as conductive supports to both anchor electrocatalysts and modulate the electrochemical reactions in a controlled fashion[15,16]. The combination of the high surface area (theoretical value of 2630 m^2/g), high conductivity, unique graphitic basal plane structure and potential low manufacturing cost makes graphene a promising candidate for catalyst support in fuel cells[17]. It is expected that graphene research will offer a new type of carbon-metal nanocomposite for the next generation of catalysts[15].

In this work, we employ the ALD technique to fabricate single atoms and sub-nanometer clusters of Pt on the surfaces of graphene nanosheet support. The morphology, size, density and loading of Pt on graphene can be precisely controlled by simply adjusting the number of ALD cycles. High angle annular dark field scanning TEM (HAADF-STEM) and electrochemical characterizations were carried out to determine how the catalyst structure changes with adjusting the numbers ALD cycles, and how it affects the MOR activity and CO adsorption. X-ray Absorption Fine Structure (XAFS) spectroscopy at the Pt $L_{3,2}$ edge, including both the X-ray Absorption Near Edge Structure (XANES) and the Extended X-ray Absorption Fine Structure (EXAFS), revealed the correlation of the electronic structure and local environment of Pt and their electrochemical performance.

Results

Preparation of single-atom platinum catalyst on graphene via ALD technique. The graphene nanosheet (GNS) support was prepared using the procedure described previously[18] which involves graphite oxidation, thermal exfoliation, and chemical reduction. Fig. S2 shows the SEM (a) and TEM (b) images of graphene. It can be seen that the material is transparent with the voile-like structure and consists of randomly crumpled sheets closely associated with each other, forming a disordered solid. The planar sheets are clearly observed, indicating the features of high surface/volume ratio and the two-dimensional structure of graphene.

Platinum was deposited on graphene supports by ALD using the (methylcyclopentadienyl)-trimethylplatinum ($MeCpPtMe_3$, Aldrich, purity 98%) and oxygen (99.999%) as precursors, and nitrogen (99.9995%) as purge gas[10,11]. ALD of Pt follows a similar pathway as CVD of Pt[19] during the oxidative decomposition of $MeCpPtMe_3$, but separating into two half reactions:

1st half reaction:

$$\text{Pt-O}^* + (\text{MeCp})\text{Pt}(\text{CH}_3)_3 \rightarrow (\text{CH}_3)_2\text{Pt}(\text{MeCp})^* + \text{CO}_2\uparrow + \text{H}_2\text{O}\uparrow + \text{fragments} \quad (1)$$

2nd half reaction:

$$(\text{CH}_3)_2\text{Pt}(\text{MeCp})^* + \text{O}_2 \rightarrow \text{Pt-O}^* + \text{CO}_2\uparrow + \text{H}_2\text{O}\uparrow + \text{fragments} \quad (2)$$

Here, '*' represents an active surface species, and Pt-O* represents oxygen molecules (or dissociated oxygen ions) that are adsorbed on the Pt surface. As shown in Fig. 1, there exists a monolayer of oxygen containing function group on the surface of graphene nanosheets (a). During the $MeCpPtMe_3$ exposure, some of the precursor ligands react with the adsorbed oxygen, to form CO_2, H_2O and hydrocarbon fragments (eq. 1). The limited supply of surface oxygen prevents all of the ligands from oxidizing and provides the self-limiting growth necessary for ALD, creating a Pt containing monolayer (b). The subsequent oxygen exposure forms a new adsorbed oxygen layer on the Pt surface (eq. 2) (c). This two processes form a complete ALD cycle. Through tuning the number of ALD cycles, the Pt deposition can be precisely controlled. This mechanism is supported by quadrupole mass spectrometry (QMS) measurements in which CO_2 and H_2O were observed during both the $MeCpPtMe_3$ and the oxygen exposures[20].

Electron microscopy. Sub-angstrom-resolution aberration-corrected scanning transmission electron microscopy (STEM) was used to characterize the dispersion and configuration of Pt single atoms and clusters on the GNS. The instrument is fitted with a Super-Twin lens and two aberration correctors in order to achieve sub-angstrom resolution both for phase contrast imaging and STEM. Individual heavy atoms in practical catalysts can be discerned with atomic resolution in high angle annular dark field (HAADF) images[8].

Structure characterization reveals that ALD is an efficient method to deposit highly dispersed Pt particles on the surface of graphene nanosheet. Fig. S3a–c show the SEM images of Pt on graphene prepared with 50, 100 and 150 ALD cycles, respectively. The corresponding TEM images are shown in Fig. S3a′–c′. We can see that discrete and well dispersed Pt nanoparticles have been uniformly deposited on the surface of the graphene nanosheets. The Pt nucleation density, as illustrated by the number of particles counted in a unit area of graphene nanosheets, increases with the cycle numbers. A few hundred particles were randomly measured under TEM to obtain the particle size distributions. The Pt particles, displaying an average size of 0.5 nm, 1–2 nm and 2–4 nm, respectively, are uniformly distributed on graphene nanosheet supports with 50, 100 and 150 ALD cycles (50ALDPt/graphene, 100ALDPt/graphene and 150ALDPt/graphene). Consequently, the Pt loading on graphene also increases from 1.52, to 2.67 and 10.5 wt%, which were confirmed by ICP-OES. The HRTEM images (Fig. S4a–c and their insets) reveal that each Pt nanoparticle or cluster is single crystalline and arranged in the cubic close-packed structure. Especially, as shown in Fig. S4a and its inset, Pt clusters that consist of only/less than ten atoms are assembled into a closely packed crystal structure. This indicates the crystalline nature of Pt cluster in the early stage of ALD growth.

To further investigate the details of ALD Pt on graphene, sub-angstrom-resolution, aberration-corrected STEM was used to characterize the Pt clusters on graphene. Atomic resolution HAADF images were proven previously to be an efficient way to study individual heavy atoms in catalysts[7,21,22]. Fig. S5a and b show the bright-field TEM image and HAADF-STEM image of Pt/graphene with 100 ALD cycles, respectively. On the bright-field TEM image, only Pt nanoparticles of 1–4 nm in size are observed (Fig. S5a). Interestingly, the sensitivity to atomic number Z-contrast of HAADF-STEM revealed that in addition to these Pt nanoparticles, the presence of numerous individual Pt atoms, as well as very small Pt clusters of size $\leq$1 nm consisting of only a few atoms (Fig. S5b). Fig. S6a and S6b show respectively the EDS spectra and the corresponding HAADF-STEM image of Pt/graphene. The EDS spectra were collected from five different areas with Pt-clusters ranging from 1.2 to 6.7 nm size on a graphene nanosheet as well as an area containing only a few atoms. The presence of Pt and C is confirmed by all measurements.

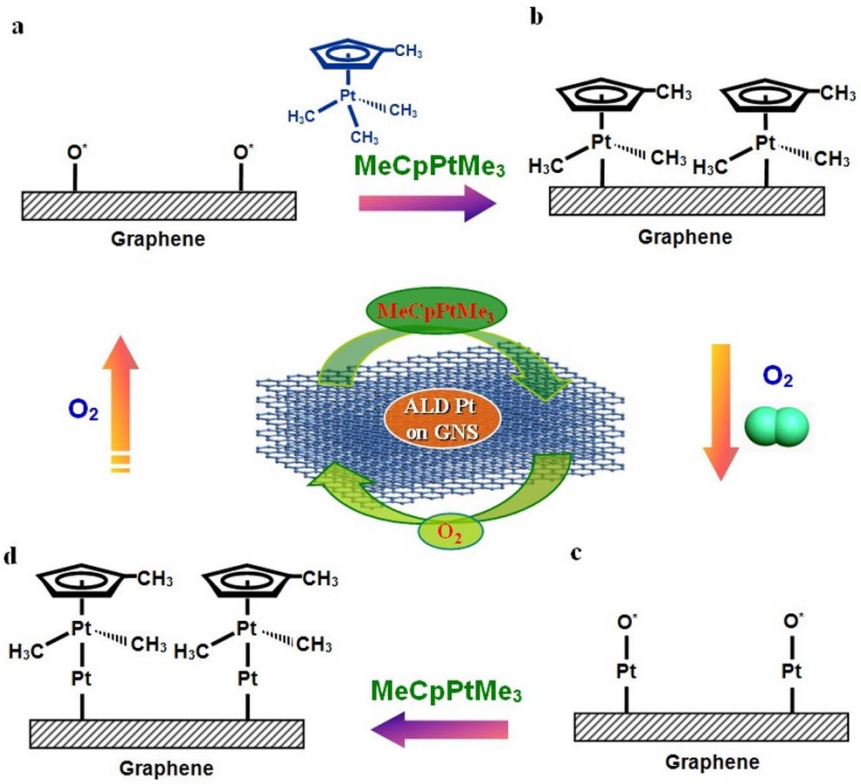

Figure 1 | Schematic illustrations of Pt ALD mechanism on graphene nanosheets. (a) There exists a monolayer of oxygen containing function group on the surface of graphene nanosheets; (b) during the $MeCpPtMe_3$ exposure, some of the precursor ligands react with the adsorbed oxygen, and the limited supply of surface oxygen provides the self-limiting growth necessary for ALD, creating a Pt containing monolayer; (c) the subsequent oxygen exposure forms a new adsorbed oxygen layer on the Pt surface; This two processes (b and c) form a complete ALD cycle, producing one atomic layer of Pt atoms. Through tuning the number of ALD cycles (d), the Pt deposition can be precisely controlled. Here, '*' represents an active surface species, and Pt-O* represents oxygen molecules (or dissociated oxygen ions) that are adsorbed on the Pt surface.

The Cu peak is attributed to the Cu mesh on which the catalyst is dispersed for TEM measurement. This further indicates that the bright spots in the HAADF-STEM image are individual Pt atoms and subnanometer Pt clusters anchored to the surface of the graphene nanosheets. The peak intensities were normalized according to the Cu $K_{\alpha 1}$ intensity. We can see that all areas show obvious Pt signals, even areas where only a few Pt atoms are present, and a decrease of particle size results in a decrease of the Pt peaks intensity. It is inferred that these individual atoms and subnanometer-sized clusters of Pt observed for the first time with appreciable amounts must be connected to the unprecedented MOR performance of Pt catalyst deposited using ALD[15].

The size and deposition density of Pt on graphene could be easily moderated via controlling the ALD cycles. Fig. 2 shows the HAADF-STEM images, at different magnifications, of Pt on graphene with three different ALD cycles. For the Pt/graphene sample after undergoing 50 ALD cycles, Fig. 2a and a′ clearly show that single atoms of Pt (bright spots on the dark background) are dominantly distributed on the surface of graphene nanosheets. Occasionally, subnanometer Pt clusters and nanoparticles with size of 1–2 nm can also be found, which is consistent with the bright field TEM investigations. After 100 cycles (Fig. 2b and b′), some clusters appear to be larger, forming nanoparticles with two groups of average size of 1 nm and 2 nm respectively, while many single atoms and clusters were observed, similar to that for the 50-cycle sample (Fig. 2a and a′). It is believed that the single atoms existing from the 50-cycle sample have grown, creating the relative larger clusters and particles, while at the same time, newer single atoms have formed. Finally, after 150 cycles (Fig. 2c and c′), in addition to the newly formed single atoms and clusters, some existing clusters and particles from the 50- and 100-cycle samples appear to be even larger with three groups of sizes with 1, 2 and 4 nm, respectively. SEM, TEM and HAADF-STEM images of the three Pt/graphene samples with different ALD cycles reveal that the deposited Pt form disperse particles, growing from individual single atoms and subnanometer clusters via the agglomeration in a cubic closely pack manner, instead of layer-by-layer growth. Many single atoms can be seen on each of the sample in addition to these particles. Previous studies have observed that the thin-film growth rate increases after a Pt seed is formed[23]. This growth rate increase has been attributed to a higher affinity for $MeCpPtMe_3$ adsorption and decomposition on Pt sites[24].

These findings raise key issues for fabricating Pt single atoms or sub-nanometer clusters on graphene and other support materials by using ALD. One of the key issues is the chemical state of ALD Pt at the early stage. The conversion of Pt from the oxidation state in $MeCpPtMe_3$ precursor to the zero-valent metallic chemical state on graphene offers promising opportunities to employ ALD-grown metal nanostructures for catalysis and fuel cell applications.

The presence of Pt individual atoms and extremely small clusters suggests a strong interaction between graphene and Pt atoms, which may induce some modulation in the electronic structure of the Pt clusters. Okamoto et al. have reported, based on density-functional theory (DFT) calculation, that introducing a carbon vacancy into a graphene sheet enhances the interaction between graphene and Pt_{13} clusters[25]. They concluded that the stability of the metal clusters on graphene with carbon vacancies was higher than that on defect-free graphene. The graphene used in this study must exhibit many carbon vacancies and defects, due to the preparation method by chemical reduction of exfoliated graphite oxide sheets. It is thus expected that carbon atoms with dangling bond or oxygen-containing functional

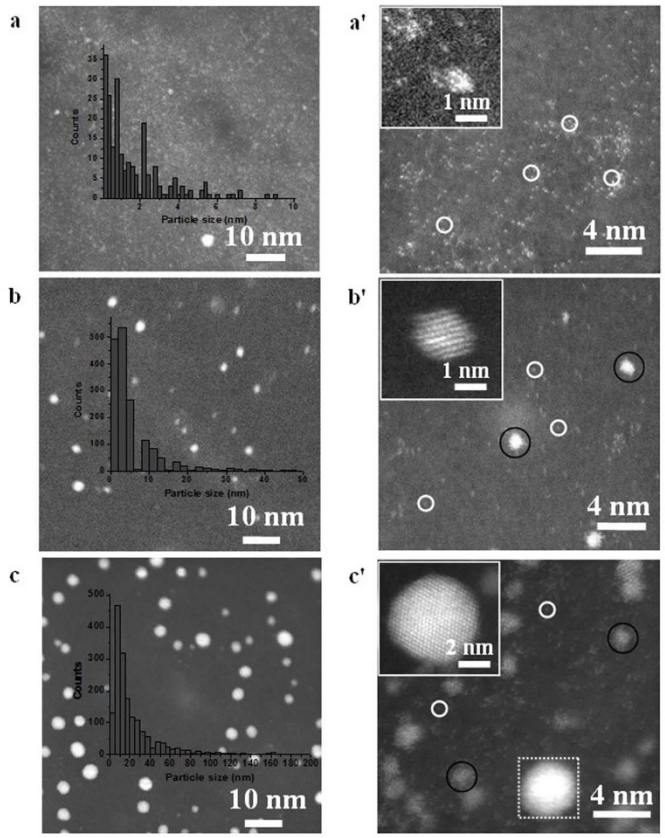

Figure 2 | HAADF-STEM images of Pt/GNS samples. (a, b, c) present the results with 50, 100, and 150 ALD cycles, respectively, and (a′, b′, c′) show the corresponding magnified images. Inset in each figure show the corresponding histogram of Pt on GNS.

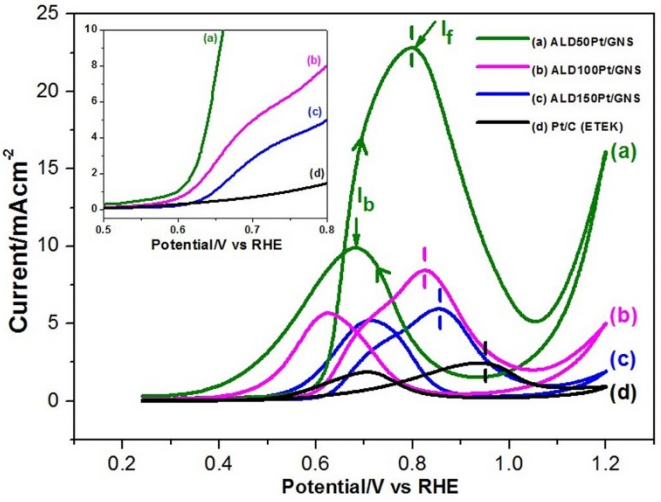

Figure 3 | CVs of methanol oxidation on (a) ALD50Pt/GNS, (b) ALD100Pt/GNS, (c) ALD150Pt/GNS, (d) Pt/C. The inset is the enlarged CV curves at the onset potential region of the methanol oxidation on different catalysts. The peak potentials for methanol oxidation of Pt/GNS increases with the increase of ALD cycles: 50 cycles (0.79 V) < 100 cycles (0.82 V) < 150 cycles (0.85 V) < Pt/C (0.96 V) (vs. RHE). The negative shifts of the onset and peak potentials indicate that the ALDPt/GNS catalysts are able to significantly reduce the overpotential for methanol oxidation. Further, the methanol oxidation peak current density indicates that ALD50Pt/GNS is 4 and 2.7 times more active than ALD100Pt/GNS and ALD100Pt/GNS, respectively. Most importantly, all ALDPt/GNS catalysts exhibit several times higher activity for MOR than that of Pt/C catalyst, especially, ALD50Pt/GNS is over 9.5 times more active than of Pt/C catalyst.

groups exist at the defect sites of the graphene nanosheets used in this work. The Pt precursor used in this study reacts with these defects. The present study indicates that graphene can be anticipated as a new type of carbon support material, modifying catalytic properties of Pt as fuel cell catalysts.

Catalytic performance. We used the methanol oxidation reaction (MOR) to investigate the catalytic performance of ALDPt/GNS samples; as such reaction is at the heart of DMFC technology. Cyclic voltammetry (CV) was used to systematically study the catalytic activity and the onset potential of methanol oxidation of the catalysts. A better catalyst is characterized by a higher induced current density at a given applied potential or a lower onset potential. Fig. 3 shows the CVs for MOR on Pt/graphene samples with different ALD cycles and Pt/C (ETEK) catalyst. Two typical oxidation peaks appear on the CV curves of all the four catalysts, arising from the oxidations of methanol and their intermediates[26]. As shown in the inset, the onset potentials of methanol oxidation are 0.59, 0.60, 0.62 and 0.7 V (vs. RHE) for ALD Pt/graphene with 50, 100 and 150 cycles, as well as Pt/C, respectively. Obviously, the peak potentials for methanol oxidation in the forward scan of Pt/graphene composites increases with the number of ALD cycles with the order of 50 cycles (0.79 V) < 100 cycles (0.82 V) < 150 cycles (0.85 V) (vs. RHE), all of which show significant negative shift than that for Pt/C (0.96 V vs. RHE). The negative shifts of the onset and peak potentials indicate that ALD Pt/GNS catalysts, especially the 50ALDPt/GNS, are able to significantly reduce the over-potential for methanol oxidation than Pt/C commercial catalyst. These improvements may be attributable to the presence of oxygen containing functional groups on graphene nanosheet as the graphene used in this study involves preparation-induced defects[25]. The methanol oxidation peak current density for 50ALDPt/GNS is 22.9 mAcm^{-2}, which is 4 and 2.7 times those of 100ALDPt/GNS (8.48 mA cm^{-2}) and 150ALDPt/GNS (5.73 mA cm^{-2}) catalysts, respectively. Interestingly, the 50ALDPt/GNS shows 9.5 times higher current density than that of ETEK Pt/C catalyst (2.41 mA cm^{-2}). The enhancement may be attributed to the intrinsic nature of Pt single atoms and sub-nanometer clusters[8] as well as the carbons substrate materials[25]. Goodenough et al.[27] suggested the anodic peak in the reverse scan to be linked to the removal of the incomplete oxidized carbonaceous species, such as CO, $HCOO^-$ and HCO^-, accumulated on the catalyst surface during the forward anodic scan. CO, a critical intermediate of methanol oxidation, can poison Pt catalyst, causing a lower fuel cell potential and energy conversion efficiency. Consequently, the ratio of the forward anodic peak current density (I_f) to the backward anodic peak current density (I_b), I_f/I_b, can be used to indicate the CO tolerance of the catalyst[27]. A low I_f/I_b value usually indicates poor oxidation of methanol to CO_2 during the forward anodic scan and excessive accumulation of residual carbon species on the catalyst surface. On the other hand, a higher I_f/I_b ratio is indicative of improved CO tolerance. In our study, Pt/graphene with 50 ALD cycles shows much higher I_f/I_b value (2.23) than that for 100 (I_f/I_b = 1.51) and 150 (I_f/I_b = 1.13) Pt cycles and Pt/C (I_f/I_b = 1.2). This suggests that methanol molecules can be more efficiently oxidized on 50ALDPt/GNS during the forward scan, generating much less poisoning species as compared to 100ALDPt/GNS, 150ALDPt/GNS and Pt/C catalysts, indicating a much better CO tolerance. Chronoamperometry data were recorded at 0.7 V (vs. RHE) for 1200 s as a measure of the catalyst deactivation (Fig. S7). We observed that the current density of four catalysts degrades with increasing time during the methanol oxidation reaction, but

ALDPt/GNS samples exhibited a slower current decay over time than commercial Pt/C catalyst, indicating better stability and higher tolerance of ALDPt/GNS to CO-like intermediates[22]. From the HAADF-STEM images of ALD 100 Pt/graphene after the stability test (Figure S8), we can see that there was only slightly increase in Pt size, but no obvious aggregation of Pt, which future indicates the excellent stability of ALD Pt/graphene catalysts in DMFCs. To further investigate the observed enhancement of CO tolerance, CO electro-stripping experiments were carried out.

More evidence on the origin of the high MOR activity and enhanced CO tolerance for Pt/graphene catalysts was obtained from CO stripping voltammetry conducted as a function of CO poisoning times in 0.5 M H_2SO_4 at room temperature. Fig. 4 shows the CO stripping voltammograms for ALDPt/GNS and Pt/C catalysts. An obvious CO oxidation peak for Pt/C was observed at 0.87 V (vs. RHE) after passing 30% CO/Ar gas for only 1 s (Fig. 4d). However, the CO oxidation peaks for the 150ALDPt/GNS, 100ALD Pt/GNS and 50ALD Pt/GNS are not observed until an exposure time of 30 s, 1 min and 2 min, respectively, was reached (Fig. 4c, b, a). Moreover, the peak potentials for CO oxidation keep nearly constant at 0.77 V (vs. RHE) for 150ALDPt/GNS and at 0.87 V (vs. RHE) for Pt/C with difference CO exposure time, while for ALDPt/GNS samples with 50 and 100 Pt cycles, the peak potentials for CO oxidation are initially at 0.72 V (vs. RHE) and steadily increase to 0.73, 0.74 and 0.77 V with time. Further, we found that the equilibrium CO coverage of all ALDPt/GNS samples was reached after passing a 30% CO/Ar gas for more than 5 min, while for the commercial Pt/C catalyst, the equilibrium CO coverage was reached after passing a 30% CO/Ar gas for 20 s. This observation indicates that the state of CO adsorption on Pt/GNS catalysts is different from commercial Pt/C catalysts[25]. The CO adsorption rates on Pt/GNS catalysts were obviously much slower compared to that on Pt/carbon black, which might be due to the superior CO tolerance of ultrafine Pt catalysts[25]. Although the detailed mechanism of the CO poisoning tolerance is not clear for the Pt/GNS catalyst, it is found that the CO tolerance and adsorption rates of Pt electrocatalysts are significantly different depending on the size of Pt and the carbon support.

X-ray absorption fine structure studies. X-ray absorption near edge structure (XANES) at the Pt L_3 and L_2 edges for a series of Pt specimens are shown in Fig. 5 and Fig. S9, respectively, including three ALD samples prepared with different Pt deposition cycles, a platinum metal foil, and a Pt/C commercial catalyst. We can see that both the Pt L_3- and L_2 -edge XANES exhibit a substantial whiteline (WL), a sharp resonance in the absorption coefficient. The WL arises from dipole transition from the Pt $2p_{3/2}$ and $2p_{1/2}$ to the d band of $5d_{5/2,3/2}$, and $5d_{3/2}$, character respectively (selection rule: $\Delta l = \pm 1$, $\Delta j = \pm 1,0$) indicating that there are appreciable unoccupied densities of states (DOS) of Pt $5d_{5/2}$ and $5_{3/2}$ character just above the Fermi level in all the sample. These DOS are crucial to the catalytic performance of Pt. The non-statistical L_3 to L_2 WL intensity ratio in Pt metal (WL at the Pt L_2-edge is nearly absent) arises from the lack of unoccupied $5d_{3/2}$ states (non-statistical distribution) above the Fermi level since the Pt $d_{5/2}$ and $5d_{3/2}$ states are filled differently due to a large

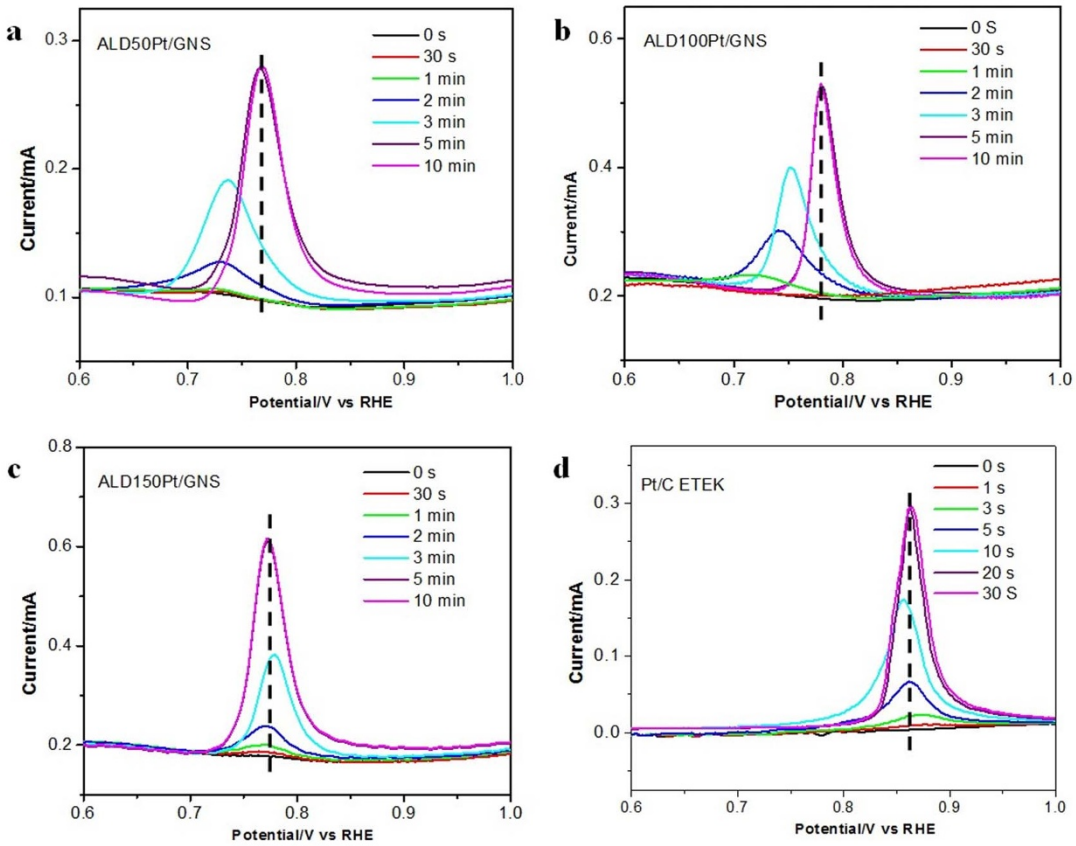

Figure 4 | The CO stripping voltammogram as a function of CO poisoning time of (a) ALD50Pt/GNS; (b) ALD100Pt/GNS; (c) ALD150Pt/GNS, (d) Pt/C, respectively. An obvious CO oxidation peak of Pt/C is observed after passing 30% CO/Ar gas for 1s (d). However, the CO oxidation peaks for ALD150Pt/GNS, ALD100Pt/GNS and ALD150Pt/GNS are not observed until an exposure time of 30 s, 1 minute and 2 min, respectively, was reached (c, b, a), indicating better CO tolerance for ALDPt/GNS samples, with 50 cycles the best. Further, the equilibrium CO coverage of all ALDPt/GNS samples was reached after passing a 30% CO/Ar gas for more than 5 min, while for the Pt/C, the equilibrium CO coverage was reached after passing a 30% CO/Ar gas for 20 s. The CO adsorption rate on Pt/GNS samples were obviously much slower compared to that on Pt/C, which might be due to the superior CO tolerance of ultrafine Pt catalysts.

spin-orbit coupling of the Pt 5d electrons. This anomaly and its chemical sensitivity have been addressed by Mott[28] and Sham[29].

Discussion

It is apparent from Fig. 5a and Fig. S9 that except in the case of Pt foil which has a very intense L_3-edge WL and a very weak L_2-edge WL, all other cases exhibit substantial WL intensity at both edges. Close examination reveals that the L_3-edge WL profile for the ALD Pt on graphene and Pt on carbon black exhibits a small change in that the L_3-edge white-line intensity decreases as the number of ALD cycles increases, in the order of 50ALDPt/GNS > 100ALDPt/GNS > 150ALDPt/GNS > Pt/C, which follows the same order of MOR and CO tolerance. The Pt-ALD and Pt-C Pt L_3-edge WL appear to be less intense than that of Pt metal but considerably broader with a positive energy shift in its maximum but a small negative shift in the threshold energy E_o. An increase in the WL intensity indicates a decrease in the number of electrons in the d orbital (DOS). Although surface oxidation in platinum will also increase the WL intensity, it will also shift E_0 to higher photon energy. The fact that a negative E_0 in the ALD samples relative to the Pt foil and Pt/C (inset of Figure 5a) indicates that the Pt in the ALD samples is essentially metallic. Therefore, the increase of the whiteline intensity in ALD samples compared to Pt/C can only indicate a stronger interaction between graphene nanosheet and Pt pushing the DOS maximum to higher energy[17]. Furthermore, a lower ALD cycle number with a relatively more intense whiteline (more available unoccupied 5d states) could mean more single Pt atoms or small cluster (more Pt-graphene interaction sites) on average resulting in a broader WL. This point will be further discussed below in the examination of the Pt L_2-edge WL and the EXAFS.

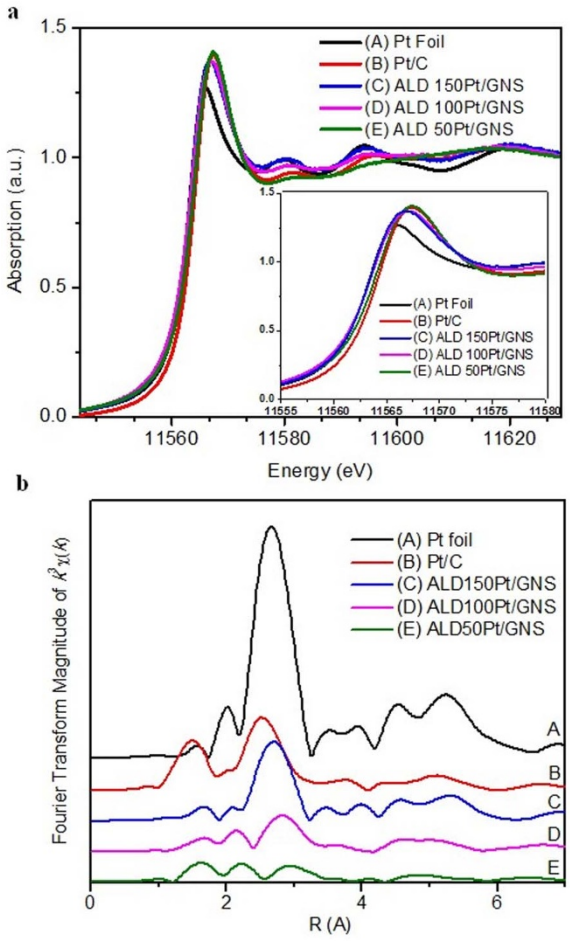

Figure 5 | X-ray absorption studies. (a) The normalized XANES spectra at Pt L_3 edge and (b) The K^3-weighted Fourier transform spectra from EXAFS of samples (A) Pt foil (black line); (B) Pt/C (red line); (C) ALD150Pt/GNS Pt/GNS (blue line); (D) ALD100Pt/GNS (magenta line); (E) ALD50Pt/GNS (olive line). Inset in A shows the enlarged spectra at Pt L_3 edge.

The corresponding L_2-edge WL (Fig. S9) exhibits considerably more variation and higher sensitivity compared to that of the Pt L_3-edge. The L_2-edge WL intensity exhibits the same trend among the Pt-ALD and Pt-C materials as observed in the L_3-edge WL; i.e. that 50ALDPt/GNS > 100ALDPt/GNS > 150ALDPt/GNS > Pt. This observation clearly confirms that for 5d noble metals such as Pt and Au, the $5d_{5/2}$ and $5d_{3/2}$ states exhibit subtle but different chemical sensitivity and that both L_3 and L_2 edge WL should be used together to address the chemistry[30,31].

To further explore the implication of the unoccupied densities of 5d states in Pt and Pt based materials, we have conducted a WL intensity analysis. It has been shown that for heavy noble metals like Pt and Au, the spin-orbit of the 5d orbital is large, ~1 eV, therefore the *j* (spin-orbit) is a better quantum number than *l (orbital)* and the d band width upon band formation in a nanoparticle or cluster is more of a quadrature of the band term and the spin-orbit term. Thus, in nearly full or full 5d bands, such as in Pt and Au, respectively, the unoccupied DOS of $5d_{5/2}$ and $5d_{3/2}$ character exhibit non-statistical distribution (deviation from $2j + 1$ multiplicity ratio, 6/4 = 3/2). Furthermore, the dipole selection rule can also modify the non-statistical ratio of the WL intensity. Since the Au d band is fully occupied, we can obtain the Pt L_3-edge WL intensity by subtracting the corresponding XANES of that of the Au. This is shown in Fig. S10. The area under the difference curve integrated between the two vertical bars, the WL intensity, ΔA_3 and ΔA_2, can be expressed as

$$\Delta A_3 = \int \mu(Pt)_{L_3 WL} - \mu(Au)_{L_3 WL}$$

$$\Delta A_2 = \int \mu(Pt)_{L_2 WL} - \mu(Au)_{L_2 WL}$$

The area under the curve thus obtained is listed in table 1 together with other relevant parameters. It should be noted that the Pt L_2-edge WL is probing only the unoccupied states of $5d_{3/2}$ character while the L_3-edge WL is probing both the Pt $5d_{5/2}$ and $5d_{3/2}$. Following a previous analysis procedure, we have

$$\Delta A_3 = C_o N_o E_3 \left(R_d^{2p_{3/2}}\right)^2 \left[\frac{6h_{5/2} + h_{3/2}}{15}\right]$$

$$\Delta A_2 = C_o N_o E_2 \left(R_d^{2p_{1/2}}\right)^2 \left(\frac{1}{3} h_{3/2}\right)$$

Where $C_o = 4\pi^2\alpha/3$, (α is the hyperfine constant), N_o is the density of the Pt atoms and E_3 and E_2 are the corresponding edge threshold, E_o for the L_3 and L_2 edges, respectively; the R term is the radial transition matrix element. If we assume that the R terms are similar for both edges, we let $C = C_o N_o R^2$. This approximation leads to the following expressions.

$$h_{5/2} = \frac{1}{2C}\left[5\frac{E_2}{E_3}\Delta A_3 - \Delta A_2\right]$$

$$h_{3/2} = \left[\frac{3\Delta A_2}{C}\right]$$

Using the results from Pt metal and the $d_{5/2}$ and $d_{3/2}$ hole population from band structure calculations, a C value of 7.484×10^4 cm^{-1} eV was derived previously for Pt metal[30]. For the set of experimental data recorded in this work, the corresponding d hole counts are as listed in the table 1. It should be noted however, that the area under WL (the difference curve) alone can already provide an important measure for the relative DOS of the 5d holes in our system of interest. It should also be noted that the d-hole ratio is independent of the scaling factor C, which may need to be recalibrated under

Table 1 | Pt $L_{3,2}$-edge threshold and whiteline parameters

	Pt L_3-edge WL				Pt L_2-edge WL					
Sample	E_o(eV)[a]	E(eV)[b]	Γ(eV)[c]	ΔA_3[d]	E_o(eV)[a]	E(eV)[b]	Γ(eV)[c]	ΔA_2[d]	$h_{5/2}$	$h_{3/2}$
Pt foil	11563.8	11565.7	4.67	6.78	13269.5	13272.5	7.48	2.95	0.53	0.12
ALD 50 Pt/GNS	11563.6	11567.1	8.43	7.47	13269.7	13272.9	7.67	6.15	1.20	0.25
ALD100 Pt/GNS	11563.8	11567.5	8.76	6.88	13269.9	13273.1	8.24	5.31	1.13	0.21
ALD150 Pt/GNS	11563.6	11567.0	8.66	6.98	13269.5	13273.5	8.55	5.47	0.93	0.22

[a]Position of the point of inflection of the rising edge; [b]Peak position; [c]Linewidth at Half maximum of the WL, see inset of Fig. 4 a; [d]Area under the difference curve (see Fig. S10, marked by the vertical bar) for unity edge jump, the unity edge jump for the Pt L_3 and L_2 edge corresponds to a value of 2.5×10^3 cm^{-1} and 1.16×10^3 cm^{-1}, respectively.

different experimental conditions. Two important conclusions emerge from this analysis. First, the results confirm quantitatively the observation that the 50ALDPt/GNS sample has the highest total unoccupied density of states of Pt 5d character. Second, the Pt $5d_{3/2}$ state, which is nearly full in disparity to that of the Pt $5d_{3/2}$ hole in Pt metal becomes more chemically active upon dispersion into atoms or small cluster, this activity is likely due to surface and interface (Pt-graphene interaction) effects. Thus the trend of Pt 5d unoccupied densities of states correlates well with their electrocatalytic performance. More details on the spectroscopy and its implications for Pt based catalysis will be discussed elsewhere.

The oscillations beyond the whiteline exhibit the same pattern as fcc Pt. Close examination reveals that the XANES patterns observed in the Pt ALD samples grow in intensity and become sharper as the number of cycles increases, which suggests that the crystalline order increases and approaches that of Pt foil. This is in good accord with the XAFS behavior of the growth of Au nanoparticles[32].

The Fourier transforms of the EXAFS region for various cases are plotted in Figure 5b. The peak at ~1.6 Å is associated with Pt bonded to low Z elements (C or O though not distinguishable due to similar backscattering phase and amplitude as well as bond length) and the peak at ~2.6 Å reflects Pt-Pt bonding in the first coordination shell containing Pt. The peak intensity is proportional to the coordination number and related to the degree of order/disorder of the corresponding coordination shells, and the effect can be described by the Debye-Waller factor, which describes the mean square displacement of the inter-atomic distance between the absorbing atom and the backscattering atom due to vibration and static disorder (slightly different chemical environment). As shown in table 2, 150ALDPt/GNS has a fitted Pt-Pt coordination number of CN = 9.2 closest to that of the Pt metal (CN = 12) and a relatively small contribution from Pt-C or Pt-O. 100ALDPt/GNS has a much lower CN (1.5) relative to Pt metal indicating the presence of much smaller Pt cluster size on average. The contributions from Pt-C or Pt-O increase for a smaller Pt cluster (more surface Pt atom). Interestingly, though not surprisingly, the 50ALDPt/GNS sample has very strong Pt-C or Pt-O contribution, and the Pt-Pt bond distance deviates considerably from a perfect Pt metal. This observation indicates that only very small Pt cluster and single atoms dominate in the 50ALDPt/GNS sample. In all ALD samples, single Pt atom interacts with GNS through Pt-C or Pt-O bonding while smaller Pt cluster (in 100ALD and 50ALD) has more surface atoms for more extensive Pt-GNS interaction. This EXAFS observation agrees with the observation in XANES (stronger interaction corresponds to a more intense whiteline; this is more apparent at the Pt L_2-edge XANES, and single Pt atoms and small clusters exhibit nearly washed out oscillation beyond the whiteline). Smaller Pt clusters can offer more available catalytic positions per unit mass of Pt for electrochemical reaction from under-coordinated surface atom. This effect will be more obvious for single Pt atom dominated sample (for instance in 50ALDPt/GNS). The presence of single atoms and small Pt clusters will yield very disordered EXAFS as observed. The XANES, albeit weak and much broadened, still shows some metallic Pt characteristics, indicating that the local order of Pt in these small clusters is still Pt metal like.

Table 2 | XAS analysis results for the three ALD samples and reference samples

Sample	N	R (Å)	$\Delta\sigma^2$ (Å^2)
Pt foil	12.0	2.66 (±0.02)	0.0023
Pt/C	6.3 (±1.0)	2.54 (±0.02)	0.0041 (±0.0009)
ALD150Pt/GNS	9.2 (±1)	2.79 (±0.02)	0.0061 (±0.010)
ALD100Pt/GNS	1.5 (±0.3)	2.80 (±0.02)	0.0029 (±0.010)
ALD50Pt/GNS	no physical solution by fitting to crystalline Pt*		

N, coordination number for Pt-Pt bond in crystalline Pt; *R*, Pt-Pt bond length (r_{Pt-Pt}); $\Delta\sigma^2$, Debye–Waller factor. *Note: fitting ALD 50 by Pt-Pt crystalline structure doesn't have physical solution. This has to be considered as single atom dominated in ALD 50.

In conclusion, we have reported a systematic study in which ALD was used to synthesize a class of novel catalysts that consists of platinum single atoms, sub-nanoclusters, and nanoparticles uniformly deposit on the surface of graphene nanosheets. We showed that the morphology, size, density and loading of Pt on graphene can be precisely controlled by simply adjusting ALD cycle numbers. These catalysts showed much higher activity for methanol oxidation and superior CO tolerance compared to conventional Pt/C catalyst. The Pt $L_{3,2}$-edge XAFS strongly supports the electron microscopy results and reveals a correlation between the $L_{3,2}$-edge whiteline intensity and the chemical behavior for these ALDPt/GNS catalysts. The more low-coordinated and unsaturated 5d orbitals of the single Pt atoms are responsible for the excellent electrochemical performance. Our work provides a promising approach for the design of highly active next-generation catalyst based on single-atom Pt, which has a great potential to substantially reduce the high cost of fuel cells and other industries that use noble metals as catalysts.

Methods

ALD synthesis of Pt on graphene. Platinum was deposited on graphene supports by ALD (Savannah 100, Cambridge Nanotechnology Inc., USA). The container for graphene was placed inside the reactor directly on the heated stage of ALD. The deposition temperature was 250°C, while the container for the Pt precursor was kept at 65°C to provide a steady state flux of $MeCpPtMe_3$ to the reactor (~800 mTorr at 65°C)[11]. Gas lines were held at 100–150°C to avoid precursor condensation. High-purity O_2 (99.999%) was used as the counter reactant, and high-purity N_2 (99.9995%) was used as both a purging gas and carrier gas. In each ALD cycle, 1 s of $MeCpPtMe_3$ pulse and 5 s of O_2 pulse were separated by 20 s of N_2 purge. The Pt loading on graphene was accurately controlled by the number of ALD cycles, and was further confirmed by inductively coupled plasma-optical emission spectroscopy (ICP-OES).

Physical characterization. The morphologies and microstructures of the as-prepared samples were examined by scanning electron microscopy (SEM, Hitachi S-4800) operated at 5 kV. Subangstrom-resolution aberration-corrected scanning transmission electron microscopy (STEM, FEI Titan 80–300 Cubed TEM) was used to characterize the dispersion and configuration of Pt clusters and single atoms on graphene. The instrument was operated at 200 keV with a convergence angle of 21mrad and HAADF images were taken at a Camera Length of 115 mm. The instrument is fitted with a Super-Twin lens and two hexapole aberration correctors

(one for the image-forming lens and one for the probe-forming lens) in order to achieve sub-angstrom resolution both for phase contrast imaging and STEM. The probe diameter is less than 0.1 nm achieved with a high-brightness electron source. The sample was tilted towards the energy-dispersive X-ray detector in order to increase the counts in the X-ray spectra.

Electrochemical measurements. The working electrodes were prepared with a procedure similar to the one reported previously[33]. Typically, the catalyst dispersions were prepared by mixing 5 mg of catalyst in 5 mL aqueous solution containing 1 mL of isopropyl alcohol and 30 mL of 5 wt% Nafion solution followed by 12 min ultrasonication. Glassy carbon (GC) disk electrodes (5 mm diameter, 0.196 cm^2, Pine Research Instrument) served as the substrate and were polished to a mirror finish. An aliquot of catalyst suspension was pipetted onto the GC disk substrate to obtain the same Pt loadings for all catalysts. The catalyst films were dried under flowing N_2 at room temperature. The electrochemical properties of the catalysts were test on an Autolab potentiostat/galvanostat (Model, PGSTAT-30, Eco-chemie, Brinkman Instruments) with rotation control (MSR, Pine Instruments) using a three-electrode system that consists of a GC rotating disk electrode (RDE), a Pt wire counter electrode, and a Ag/AgCl (3 M NaCl) reference electrode separated from the working electrode compartment by a closed electrolyte bridge. For convenience, all potentials in this study are referenced to the reversible hydrogen electrode (RHE). The working electrode was first cycled between 0 and 1.2 V at a scan rate of 50 mVs^{-1} for 50 times in an Ar-purged H_2SO_4 solution (0.5 M) at room temperature until a clean electrode surface was obtained. Cyclic voltammetry (CV) measurements were conducted by cycling the potential between 0 and 1.2 V, with a sweep rate of 50 mVs^{-1}. For methanol oxidation reaction (MOR), the CVs were measured in an air-free aqueous solution containing 1 M MeOH and 0.5 M H_2SO_4 at room temperature in an Ar atmosphere. For CO stripping voltammetry, 30%CO/N_2 gas was purged into the solution at a position close to the working electrode for 1 s to 20 min, with the electrode polarized at 0.05 V versus RHE in a fume hood. The excess CO was purged with Ar for 30 min under potential control followed by CO stripping at a scan rate of 50 mVs^{-1}.

X-ray absorption spectroscopy. The Pt $L_{3,2}$-edge adsorption spectra X-Ray Absorption Fine Structure (XAFS) measurements were performed on the 06ID superconducting wiggler sourced hard X-ray microanalysis (HXMA) beamline at the Canadian Light Source with a premirror - double crystal monochromator – postmirror configuration using Si (111) crystals and Rh mirrors. When the data was collected, the CLS 2.9 GeV ring was operated at 250 mA injection current and the beamline wiggler was running at 1.9 T. Measurements were made at room temperature in transmission mode for Pt foil and for the sample Pt/C with ion chambers filled with 20% of Ar and 80% of He, and in fluorescence mode for the ALD system using a 32- element Ge detector. The spectrum acquisition was set at 10 eV/step, 0.5 eV/step, and 0.05 $Å^{-1}$/step for the pre-edge, XANES, and EXAFS regions, respectively. The second crystal of the monochromator was 60% detuned during the data collection to suppress the higher harmonic components. Metal Pt foil (Pt L_3 edge) was used for mono energy calibration. The Pt $L_{3,2}$-edge XANES, as well as Pt L_3-edge EXAFS were recorded for the analysis. The software package ATHENA version 0.8.056 was used for data reduction. Software TkAtom version 3.0beta7 was used to generate the FEFF7.02 input files, and WinXAS version 3.0 was used for R space fitting based on the FEFF modeling for the Pt metal and PtO_2.

1. Chen, A. & Holt-Hindle, P. Platinum-based nanostructured materials: synthesis, properties, and applications. *Chem. Rev.* **110**, 3767–3804 (2010).
2. Borup, R. *et al*. Scientific aspects of polymer electrolyte fuel cell durability and degradation. *Chem. Rev.* **107**, 3904–3951 (2007).
3. Chen, Y. *et al*. Atomic layer deposition assisted Pt-SnO_2 hybrid catalysts on nitrogen-doped CNTs with enhanced electrocatalytic activities for low temperature fuel cells. *Int. J. Hydrogen Energy.* **36**, 11085–11092 (2011).
4. McGrath, K. M., Prakash, G. K. S. & Olah, G. A. Direct methanol fuel cells. *J. Ind. Eng. Chem.* **10**, 1063–80 (2004).
5. Li, H. Q. *et al*. Rechargeable Ni–Li battery integrated aqueous/nonaqueous system. *J. Am. Chem. Soc.* **131**, 15098–15099 (2009).
6. Hogarth, M. P. & Ralph, T. R. Catalysis for low temperature fuel cells PART III: challenges for the direct methanol fuel cell. *Platinum Metals Rev.* **46**, 146–164 (2002).
7. Qiao, B. *et al*. Single-atom catalysis of CO oxidation using Pt_1/FeO_x. *Nature Chem.* **3**, 634–641 (2011).
8. Uzun, A., Ortalan, V., Hao, Y., Browning, N. D. & Gates, B. C. Nanoclusters of gold on a high-area support: almost uniform nanoclusters imaged by scanning transmission electron microscopy. *ACS Nano* **3**, 3691–3695 (2009).
9. Christensen, S. T. *et al*. Controlled growth of platinum nanoparticles on strontium titanate nanocubes by atomic layer deposition. *Small* **5**, 750–757 (2009).
10. King, J. S. *et al*. Ultralow loading Pt nanocatalysts prepared by atomic layer deposition on carbon aerogels. *Nano Lett.* **8**, 2405–2409 (2008).
11. Liu, C., Wang, C. C., Kei, C. C., Hsueh, Y. C. & Perng, T. P. Atomic layer deposition of platinum nanoparticles on carbon nanotubes for application in proton-exchange membrane fuel cells. *Small* **5**, 1535–1538 (2009).
12. Yu, X. W. & Ye, S. Y. Recent advances in activity and durability enhancement of Pt/C catalytic cathode in PEMFC. *J. Power Sources* **172**, 145–154 (2007).
13. Liao, S., Holmes, K.-A., Tsaprailis, H. & Briss, V. I. High performance PtRuIr catalysts supported on carbon nanotubes for the anodic oxidation of methanol. *J. Am. Chem. Soc.* **128**, 3504–3505 (2006).
14. Geim, A. K. & Novoselov, K. S. The rise of graphene. *Nature. Mater.* **6**, 183–191 (2007).
15. Yoo, E. *et al*. Enhanced electrocatalytic activity of Pt subnanoclusters on graphene nanosheet surface. *Nano. Lett.* **9**, 2255–2259 (2009).
16. Shao, Y. *et al*. Highly durable graphene nanoplatelets supported Pt nanocatalysts for oxygen reduction. *J. Power Sources* **195**, 4600–4605 (2010).
17. Tang, L. *et al*. Preparation, structure, and electrochemical properties of reduced graphene sheet films. *Adv. Funct. Mater.* **19**, 1–8 (2009).
18. Hummers, W. S. & Offeman, R. E. Preparation of graphite oxide. *J. Am. Chem. Soc.* **80**, 1339–1339 (1958).
19. Xue, Z., Thridandam, H., Kaesz, H. D. & Hicks, R. F. Organometallic chemical vapor deposition of platinum. Reaction kinetics and vapor pressures of precursors. *Chem. Mater.* **4**, 162–166 (1992).
20. Aaltonen, T., Rahtu, A., Ritala, M. & Leskela, M. Reaction mechanism studies on atomic layer deposition of ruthenium and platinum. *Electrochem. Solid-State Lett.* **6**, C130–C133 (2003).
21. Herzing, A. A., Kiely, C. J., Carley, A. F., Landon, P. & Hutchings, G. J. Identification of active gold nanoclusters on iron oxide supports for CO oxidation. *Science* **321**, 1331–1335 (2008).
22. Ortalan, V., Uzun, A., Gates, B. C. & Browning, N. D. Direct imaging of single metal atoms and clusters in the pores of dealuminated HY zeolite. *Nature Nanotech.* **5**, 506–510 (2010).
23. Knoops, H. C. M. *et al*. Remote plasma ALD of platinum and platinum oxide film. *Electrochem. Solid State Lett.* **12**, G34–G36 (2009).
24. Takakusagi, S., Fukui, K., Tero, R., Nariyuki, F. & Iwasawa, Y. Self-limiting growth of Pt nano-particles from $MeCpPtMe_3$ adsorbed on TiO_2(110) studied by STM. *Phys. Rev. Lett.* **91**, 066102 (4 pages) (2003).
25. Okamoto, Y. Density-functional calculations of icosahedral M_{13} (M = Pt and Au) clusters on graphene sheets and flakes. *Chem. Phys. Lett.* **420**, 382–386 (2006).
26. Che, G., Lakshmi, B. B., Fisher, E. R. & Martin, R. Carbon nanotubule membranes for electrochemical energy storage and production. *Nature* **393**, 346–349 (1998).
27. Manohara, R. & Goodenough, J. B. Methanol oxidation in acid on ordered NiTi. *J. Mater. Chem.* **2**, 875–887 (1992).
28. Mott, N. F. The basis of the electron theory of metals, with special reference to the transition metals. *Proc. Phys. Soc. (London), A* **62**, 416–421 (1949).
29. Sham, T. K., Naftel, S. J. & Coulthard, I. $M_{3,2}$-edge x-ray absorption near-edge structure spectroscopy: An alternative probe to the $L_{3,2}$-edge near-edge structure for the unoccupied densities of d states of 5d metals. *J. Appl. Phys.* **79**, 7134–7138 (1996).
30. Matthesis, L. M. & Deitz, R. E. Relativistic tight-binding calculation of core-valence transitions in Pt and Au. *Phys. Rev. B* **22**, 1663–1676 (1980).
31. Kuhn, M. & Sham, T. K. Charge redistribution and electronic behavior in a series of Au-Cu alloys. *Phys. Rev. B* **49**, 1647–1661(1994).
32. Zhang, P. & Sham, T. K. X-Ray studies of the structure and electronic behavior of alkanethiolate-capped gold nanoparticles: the interplay of size and surface effects. *Phys. Rev. Lett.* **90**, 245502–245505 (2003).
33. Sun, S. H. *et al*. A new highly durable Pt nanocatalyst for PEM fuel cells: the multiarmed star-like nanowire single crystal. *Angew. Chem. Int. Ed.* **50**, 422–426 (2011).

Acknowledgments

This research was supported by Natural Sciences and Engineering Research Council of Canada (NSERC), Ballard Power System Inc., Canada Research Chair (CRC) Program, Canada Foundation for Innovation (CFI), Ontario Research Fund (ORF), Ontario Early Researcher Award (ERA) and the University of Western Ontario. S.S. thanks the NSERC CGS scholarship. G.Z. is grateful to the NSERC PDF scholarship. Part of the electron microscopy work was carried out at the Canadian Centre for Electron Microscopy, a national facility supported by NSERC and McMaster University. XAFS experiment described in this paper was performed at the Canadian Light Source (CLS), which is supported by the NSERC, the National Research Council Canada (NRC), the Canadian Institutes of Health Research, the Province of Saskatchewan, Western Economic Diversification Canada, and the University of Saskatchewan.

Author contributions

S.S. performed the catalyst preparation, characterizations and catalytic tests. N.G. conducted the STEM examinations and analyses. N.C., J.Z., S.Y., W.C., M. B. and T.S. carried out measurements and data analyses of EXAFS and contributed to writing the EXAFS sections. G.Z. and X.M. helped with ALD process. D.G. prepared the graphene support. G.Z. and R.L. contributed to TEM characterization. S.S. and G.Z. designed the study, analyzed the data and co-wrote the paper. X.S., S.Y. and S.K. proposed, planned and designed the project. X.S., G.B. and T.S. supervised the project. All authors reviewed the manuscript.

Additional information

Supplementary information accompanies this paper at http://www.nature.com/scientificreports

Competing financial interests: The authors declare no competing financial interests.

How to cite this article: Sun, S.H. *et al*. Single-atom Catalysis Using Pt/Graphene Achieved through Atomic Layer Deposition. *Sci. Rep.* **3**, 1775; DOI:10.1038/srep01775 (2013).